Mon. Not. R. Astron. Soc. **000**, 000–000 (0000) Printed 10 December 2015 (MN LATEX style file v2.2)

Gravity as the main driver of non-thermal motions in massive star formation

A. Traficante[1⋆], G. A. Fuller[1], R. Smith[1], N. Billot[2], A. Duarte-Cabral[3], N. Peretto[4], S. Molinari[5] and J. E. Pineda[6]

[1] *Jodrell Bank Centre for Astrophysics, School of Physics and Astronomy, University of Manchester, Oxford Road, Manchester M13 9PL, UK*
[2] *Instituto de Radio Astronomìa Milimètrica, Granada, Spain*
[3] *School of Physics and Astronomy, University of Exeter, Stocker Road, Exeter EX4 4QL, UK*
[4] *School of Physics and Astronomy, Cardiff University, Queens Buildings, The Parade, Cardiff CF24 3AA, UK*
[5] *IAPS - INAF, via Fosso del Cavaliere, 100, I-00133 Roma, Italy*
[6] *Max-Planck-Institut fur extraterrestrische Physik (MPE), Giebenbachstrasse 1, D-85741 Garching, Germany*

arXiv:1511.03670v2 [astro-ph.GA] 9 Dec 2015

10 December 2015

ABSTRACT

The origin of non-thermal motions in massive star forming regions can be ascribed to turbulence acting against the gravitational collapse, or to the self-gravity itself driving the rapid global collapse. The dependence between velocity dispersion, radius and clouds surface density found by Heyer et al. (2009), $\sigma/\mathrm{R}^{1/2} \propto \Sigma^{1/2}$, has been interpreted in terms of global collapse of clouds. In this work we demonstrate that this relation is an expression of a more general relation between accelerations. We introduce the gravo-turbulent acceleration, $a_{\rm k}$, which describe the non-thermal motions in each region, and the acceleration generated by the gravitational field $a_{\rm G}$, which is proportional to Σ. We also introduce a new coefficient, the force partition coefficient $\alpha_{\rm for}$ which is equivalent to the virial parameter but does not distinguish between collapsing and non-collapsing regions.

In this work we use the $a_{\rm k} - a_{\rm G}$ formalism in the analysis of a new sample of 16 massive starless clumps (MSCls) combined with data from the literature. We show that $a_{\rm k}$ and $a_{\rm G}$ are not independent. The non-thermal motions in each region can originate from both local turbulence and self-gravity but overall the data in the $a_{\rm k}$ vs. $a_{\rm G}$ diagram demonstrate that the majority of the non-thermal motions originate from self-gravity. We further show that all the MSCls with $\Sigma \geqslant 0.1$ g cm^{-2}) show signs of infall motions, a strong indication that the denser regions are the first to collapse. Finally, we include in the formalism the contribution of an external pressure and the magnetic fields.

1 INTRODUCTION

The origin of supersonic motions in collapsing clouds or cloud fragments[1] is a key question to address in order to understand the mechanism of massive star formation. It is unclear if the formation of massive stars occurs in pressure-confined regions, supported against a rapid collapse by a highly turbulent medium and possibly magnetic fields (McKee & Tan 2003; Tan et al. 2014), or if gravity is the driver of the observed non-thermal motion, leading to a faster, global collapse (e.g. Vazquez-Semadeni et al. 2007; Peretto et al. 2013).

Pioneering studies of star forming regions showed a significant contribution from the ambient interstellar medium (ISM) turbulence in shaping the clouds morphology. This was first summarized in the Larson's line-width size relation $\delta v \propto \mathrm{R}^{\Gamma}$, with $\Gamma = 0.38$ (Larson 1981). Later this was modified to $\Gamma = 0.5$ with $\delta v \propto \mathrm{R}^{0.5}$, consistent with early observations of giant molecular clouds (GMCs) which show that GMCs have all similar mass surface densities, Σ, and turbulence is ubiquitous in the ISM (e.g. Solomon et al. 1987; Heyer & Brunt 2004). The exponent $\Gamma = 0.5$ is expected if the interstellar medium is modeled as a turbulent fluid dominated by shocks (McKee & Ostriker 2007, and references therein) and simulations confirm that GMCs and their embedded massive clumps are shaped by supersonic motions and follow the Larson's relationship with $\Gamma = 0.5$ (e.g. Padoan & Nordlund 2002; Field et al. 2008).

More recently however the study of Heyer et al. (2009, hereafter H09) questioned the Larson relation and shows that the quantity $\sigma/R^{0.5}$ is not a constant of the clouds. H09 used data from the Boston University-FCRAO Galactic Ring Survey of ^{13}CO J= 1 – 0 emission (Jackson et al. 2006) to revise the study of the GMCs done by Solomon et al. (1987) using the ^{12}CO J= 1 – 0 emission. The latter is a tracer of low density gas, which rapidly becomes optically thick within the denser regions of the GMCs. The H09 analysis shows that the average mass surface density Σ of the clouds is not constant and $\sigma/\mathrm{R}^{0.5}$ increases as function of Σ, which we will refer to as the 'Heyer relation'.

Recent surveys of massive star forming clumps show that they span a range of surface densities (e.g. Urquhart et al. 2014;

[1] Following the definition of Kauffmann et al. (2013) we define a fragment as a substructure within a cloud such as a clump and core.

© 0000 RAS

Traficante et al. 2015) and it is still debated whether there is a surface density threshold Σ_t below which massive star formation cannot occur. Models suggest different values for Σ_t depending on the contribution of the magnetic fields, with Tan et al. (2014) suggesting Σ_t=0.1 g cm^{-2} in the presence of magnetic fields, and Krumholz & Tan (2007) deriving Σ_t=1 g cm^{-2} for non-magnetised regions. Observationally, the threshold range varies from $\Sigma_t \cong 0.05$ g cm^{-2} (e.g. Urquhart et al. 2014) to $\Sigma_t \cong 0.1 - 0.2$ g cm^{-2} (e.g. Tan et al. 2014; Traficante et al. 2015). This observed variation of mass surface density of massive clumps suggest that massive star formation regions could follow the Heyer rather than the Larson relationship.

McKee et al. (2010) suggested that the Heyer relation holds for relatively high mass surface densities, $\Sigma \geqslant 0.04$ g cm^{-2} (see also Tan et al. 2014). In regions of higher surface density self-gravity might increasingly dominate over the ambient turbulence. The observed non-thermal motions in massive regions should be attributed to increasing internal turbulence required to maintain equilibrium and slow-down the otherwise fast collapse, as predicted by the turbulent core model of massive star formation (McKee & Tan 2003).

Combing the data from H09 with a sample of massive clumps identified in IRDCs from Gibson et al. (2009), Ballesteros-Paredes et al. (2011) instead interpreted the Heyer relation as 'universal', from GMCs down to clump scales. In this model the turbulent motions, rather than opposing the gravity, are instead driven by the non-thermal motions in the collapsing clouds and cloud fragments (Ballesteros-Paredes et al. 2011). Molecular clouds and fragments are a product of the gravitational instability of the whole region and the observed large velocity dispersion are driven by the inward motions caused by the gravitational collapse in a hierarchical and chaotic fashion (Ballesteros-Paredes et al. 2011; Vázquez-Semadeni et al. 2009). In this interpretation, the supersonic velocity in clouds and cloud fragments is ultimately caused by gravity, as suggested by the Heyer relation.

In this work we will show that the Heyer relation is a result of a more general gravo-turbulent description of the collapsing mechanism in massive star forming regions. The new formalism that we introduce explains the Heyer relation as a relation between accelerations and a consequence of a global, chaotic collapse. This interpretation is corroborated by the analysis of new data and data taken from the literature.

The paper is structured as follows: in Section 2 we describe the observations of a sample of 16 MSCl identified in the IRDC survey of starless and protostellar clumps of Traficante et al. (2015) which we followed up with the IRAM 30m telescope[2] to trace the gas kinematics. In Section 3 we introduce the formalism of the gravo-turbulent description of massive star formation and the definition of gravitational and a gravo-turbulent accelerations. We also introduce a new coefficient that we define as the force partition coefficient $\alpha_{\rm for}$. Here we show that $\alpha_{\rm for}$ is equivalent to the virial parameter but can not be used to distinguish between collapsing and non-collapsing regions. In Section 4 we study the gravo-turbulent properties of our sample of MSCls. In Section 5 we show the gravo-turbulent vs. gravitational acceleration diagram of samples of GMCs, massive clumps and cores, combining our data with data taken from the literature and we discuss the implication of the results. In Section 6 we show how including the external pressure in the collapsing clouds can explain the observed increase in gravo-turbulent acceleration in GMCs. In Section 7 we discuss how the presence of strong magnetic field could not support the majority of the clumps against global collapse. Finally, in Section 8 we present our conclusions.

[2] Based on observations carried out with the IRAM 30m Telescope. IRAM is supported by INSU/CNRS (France), MPG (Germany) and IGN (Spain).

2 DATASET

The sample of MSCls have been selected from the starless catalogue of Traficante et al. (2015) . This catalogue contains 667 starless clumps associated with 389 IRDCs in the Galactic range $15^\circ \leqslant l \leqslant 55^\circ$ selected from the Peretto & Fuller (2009) IRDC catalogue and identified as compact sources in Hi-GAL, the *Herschel* far infrared survey of the Galactic plane (Molinari et al. 2010).These objects have been classified as candidate starless clumps in Traficante et al. (2015), as they are compact sources identified at 160, 250 and 350 μm with no counterparts or very weak emission at 70 μm.

The survey discussed in this work contains 16 MSCl ($300 \leqslant M \leqslant 2000$ M$_\odot$) selected to have a high surface density ($\Sigma \geqslant 0.05$ g cm^{-2}) and to be at the very early stage of star formation (luminosity mass ratio L/M$<$ 0.3). The original sample contains 18 MSCl which has been followed-up with the IRAM 30m telescope to study the dense gas kinematics observing the N_2H^+ (1-0), HNC (1-0) and HCO^+(1-0) emission lines (Traficante et al. 2015, in prep.). Here we do not include MSCl24.5 due to the emission at the source off-position which contaminated the spectral line emission, and MSCl30.4 for which two sources have been identified along the same line of sight in the gas emission that cannot be distinguished in the dust continuum data.

In this paper we analyze the results obtained from the N_2H^+ emission, an optically thin tracer of quiescent gas (Vasyunina et al. 2011) not strongly affected by infall or outflow motions. We use HCO^+ spectra to separate clumps which show signs of gravitational collapse from those which look quiescent, as HCO^+ lines are good tracers of outflows (Vasyunina et al. 2011) and infall (Fuller et al. 2005) motions. We also make use of the mass surface density of the clumps, estimated from the continuum data. For a comprehensive description of the clump properties estimated from the dust continuum and the analysis of the emission lines data we refer to Traficante et al. (2015, in prep.).

3 A GRAVO-TURBULENT DESCRIPTION OF THE MASSIVE STAR FORMATION MECHANISM

In the classical analysis of cloud stability the non-thermal motion is due to local turbulence which always acts against the gravitational collapse. The dynamics of the collapse is described by two independent variables, the kinetic energy $E_{\rm k} \propto \sigma$, where σ is the 1D observed (turbulent) velocity dispersion of the region, and the gravitational potential energy $E_{\rm G} \propto$ M/R, with M mass of the region in a radius R. The virial parameter α_{vir} describes the balance between these two energies and is the quantity which defines whether a region is stable against the collapse, defined as (Bertoldi & McKee 1992)

$$\alpha_{vir} = \frac{5\sigma^2 {\rm R}}{G{\rm M}} = 2a\frac{E_{\rm k}}{E_{\rm G}} \quad (1)$$

where G the gravitational constant and a is a constant which includes modifications due to non-spherical and inhomogeneous density distributions. Here we assume $a = 1$. If α_{vir} is greater than

a critical value α_{cr} the kinetic energy of the gas is sufficient to counterbalance a region's self-gravity and so it will expand and dissolve, if not confined by external pressure (e.g. Bertoldi & McKee 1992; McKee & Tan 2003). Supercritical regions with $\alpha_{vir} << \alpha_{cr}$ will instead collapse under their self-gravity, if not supported by other forces such as magnetic fields (Bertoldi & McKee 1992). Virial equilibrium, assumed as a state in which $E_{\rm k}$ is balanced by $E_{\rm G}$, is obtained for $\alpha_{cr} = 1$ (Tan et al. 2014). If clouds are model as non-magnetized, pressure bounded isothermal spheres then they will be unstable and collapse if their mass is larger than the Bonnor-Ebert (BE) mass which leads to $\alpha_{\rm cr,BE} \cong 2$ (see the discussion in Kauffmann et al. (2013); see also Tan et al. (2014)). A virial equilibrium state (whether for $\alpha_{vir} = 1$ or $\alpha_{vir} = 2$) is a necessary condition in the turbulent core model of massive star formation (McKee & Tan 2003) on the assumption that in massive clumps the internal motions reflect turbulence and/or magnetic fields (Tan et al. 2014).

Here we assume that in massive regions the collapse occurs in a hierarchical, global collapse which itself generates non-thermal, gravo-turbulent motion due to the chaotic collapse (as predicted by Ballesteros-Paredes et al. 2011). The observed non-thermal motion arises from *both* local turbulence *and* self-gravity and it is *not* independent from the gravitational term. This can be shown with a new formulation of the problem in which the dynamics is described in terms of accelerations $a_{\rm G}$ and $a_{\rm k}$.

The quantity $a_{\rm G} = \pi G\Sigma/5$ describes the average gravitational force per unit mass, i.e. the gravitational acceleration of the region, and is function of the mass surface density $\Sigma = {\rm M}/(\pi {\rm R}^2)$ only[3]. The kinetic term of the system is described by $a_k = \sigma^2/{\rm R}$ which also has the dimensions of an acceleration and is interpreted as the magnitude of the "gravo-turbulent" acceleration generated by the total (thermal and non-thermal) motions in the region.

The two accelerations are not mathematically independent, since the radius appear both in $a_{\rm k}$ explicitly and in $a_{\rm G}$ through the definition of the mass surface density. The physical interpretation of this connection is that gravitational collapse contributes itself at the observed gravo-turbulent acceleration.

The ratio of the gravo-turbulent acceleration and the gravitational acceleration in each region is described by the force partition coefficient $\alpha_{\rm for}$, which in this formulation replaces the virial parameter. The force partition coefficient is defined as:

$$\alpha_{\rm for} = \frac{\sigma^2}{\rm R}\frac{5}{\pi G\Sigma} = \frac{a_{\rm k}}{a_{\rm G}} \quad \Longrightarrow \quad a_{\rm k} = \alpha_{\rm for} a_{\rm G} \qquad (2)$$

The force partition coefficient is equivalent to the virial parameter α_{vir} (see Equations 1 and 2). However, the interpretation of $\alpha_{\rm for}$ is substantially different from α_{vir}. We cannot disentangle the turbulent from the gravitationally driven components in the observed $a_{\rm k}$of each region. The measured gravo-turbulent acceleration in a region with $\alpha_{\rm for} \leqslant 1$ could predominantly originates from either chaotic gravitational collapse or local turbulence supporting against the collapse, leading to two completely different star forming scenarios (see Figure 1). $\alpha_{for} = 2$ can still be taken as an upper limit for collapsing region: in the extreme case of non-thermal motion completely driven by self-gravity only in fact, $a_{\rm k}$=$a_{\rm G}$ and $\alpha_{\rm for}$=1. Therefore as long as $\alpha_{\rm for} \leqslant 2$ the majority of the observed non-thermal motion could in principle originate from the global chaotic collapse.

[3] We will interchange throughout the paper force with acceleration, where we define the acceleration as the force exercised by the medium in the region on a unit mass.

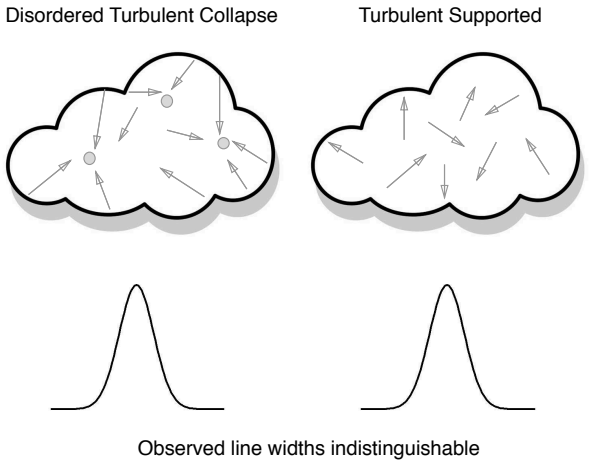

Figure 1. Cartoon of the self-gravity vs. turbulence models. *Top left*: Massive cloud with non-thermal motion generated only by the gravitational attraction of multiple centers of collapse. *Top right*: the same cloud with motion generated by random turbulence. *Bottom*: both self-gravity and turbulence generate non-thermal motion. The observed velocity dispersion (and the corresponding $a_{\rm k}$) are the same and we cannot predict the origin of the non-thermal motion.

The advantage of this formulation is the interpretation of the dynamics of a statistically significant sample of star forming regions. If the majority of the non-thermal motion in each region is gravitationally driven then as the gravitational force increases one would expect an increasing of the observed gravo-turbulent acceleration independently on the value of $\alpha_{\rm for}$ in each single cloud or cloud fragment.

In other words, if observing regions at increasing surface densities (i.e. increasing $a_{\rm G}$) we observe an increasing trend in the $a_{\rm k}$ vs. $a_{\rm G}$ diagram this demonstrates that *on average* the majority of the non-thermal motion originates from chaotic global collapse

The Heyer relation, which shows a strong indication of increasing $\sigma \propto {\rm R}^{0.5}$ with increasing mass surface density, is equivalent to the $a_{\rm k}$ vs. $a_{\rm G}$ relationship: the Heyer relationship can indeed be recovered from Equation 2 by taking the square root of both sides and imposing "virial equilibrium" (in the sense that all clouds have the same value of $\alpha_{vir} \equiv \alpha_{\rm for}$). The Heyer relation correctly connects velocity dispersion, radius and surface density of the regions but has no direct physical interpretation of these quantities. The Larson relation can also be recovered as a specific case of Equation 2. For constant $\alpha_{\rm for}$ and constant Σ, Equation 2 implies $\sigma \propto {\rm R}^{0.5}$. In other words, when the gravitational force is similar among different clouds, i.e. for similar values of the surface density of the clouds, and in condition of "virial equilibrium" than the gravo-turbulent acceleration in the system is also constant. The difference between the 0.5 power and the 0.38 power originally determined by Larson then may reflect the fact that the objects do not quite have constant surface density.

In the next Section we perform a gravo-turbulent analysis of our sample of massive clumps while in Section 5 we demonstrate that, observationally, massive clouds and cloud fragments do indeed follow Equation 1.

4 GRAVO-TURBULENT ANALYSIS OF MASSIVE STARLESS CLUMPS

The gravo-turbulent analysis and the evaluation of $\alpha_{\rm for}$ as described in Equation 2 requires the estimation of radius, mass surface density and velocity dispersion of our clumps. Table 1 summarizes the main properties of each clump.

The clump radius R is determined from the 2D-Gaussian fit of the clump dust emission done at 250 μm as R= $\sqrt{a \cdot b}$, where a and b are the two FWHMs of the 2D-Gaussian fit. The clump mass is estimated with a single-temperature greybody fit of the source fluxes at 160, 250, 350 and 500 μm from Hi-GAL and, when available, including fluxes at 870 μm from the ATLASGAL (Schuller et al. 2009) maps and at 1.1 mm from the Bolocam Galactic plane survey (BGPS, Aguirre et al. 2011) maps. The mass surface density Σ has been evaluated within the region defined by the continuum data as described in Traficante et al. (2015, in prep.). The velocity dispersion has been measured as $\sigma = \Delta v/(8\ln 2)^{1/2}$ where Δv is the velocity full width half maximum of the N_2H^+ emission. This was determined for each clump by using the CLASS task `hsf` to fit the hyperfine structure of the N_2H^+ averaged across all the pixels defined by the clump continuum data.

The non-thermal motions $\sigma_{\rm nth}$ were estimated by $\sigma_{\rm nth} = (\sigma^2_{\rm obs} - \sigma^2_{\rm th})^{1/2}$, where $\sigma_{\rm obs}$ is the 1D observed velocity dispersion and $\sigma_{\rm th}$ the thermal component of the velocity dispersion. A fixed temperature for each clump of T=10 K was adopted. This leads to $\sigma_{\rm th} \simeq 0.05$ km/s. A temperature gradient of up to $\simeq$ 10 K can be expected across starless clumps (Peretto et al. 2010; Wilcock et al. 2012). However since the average non-thermal motion of the clumps is $\sigma_{\rm nth} \simeq 0.8$ km/s, the contribution of the thermal velocity dispersion to $\sigma_{\rm obs}$ is minimal. Using T=20 K affects our results for less than 1%. The Mach number $\mathcal{M}$ is $\mathcal{M} \geqslant 2$ for all the clumps, with an average value of $\overline{\mathcal{M}} = 7.54$. All the clumps are dominated by supersonic, non-thermal motion.

The force partition coefficient is systematically lower than $\alpha_{{\rm BE},cr} = 2$ and for all but 1 source (MSCl28.7) $\alpha_{\rm for} < 1$. The average value is $\overline{\alpha}_{\rm for} \simeq 0.60$. A classical virial analysis would conclude that these MSCls are all gravitationally bound and prone to collapse, even if all of them show supersonic internal motions which could be interpreted as supersonic turbulence acting to counter-balance the gravity (Tan et al. 2014).

In the next Sections we will show how these data can be alternatively interpreted as gravity driving much of the observed non-thermal motions.

4.1 Surface density threshold for massive star formation

In order to further investigate the equilibrium properties of our sources we separate the clumps that show some sign of infall or outflow from the ones that appear quiescent. To do this we look at asymmetries in the HCO^+ spectra averaged across the whole clump defined by the dust continuum emission. HCO^+ is optically thick towards IRDCs (Sanhueza et al. 2012) and is a good tracer of outflow (Vasyunina et al. 2011) and infall (Fuller et al. 2005) motions, which are reflected as asymmetries in the line profiles. The HCO^+ spectra for all 16 clumps are showed in Appendix A. Of these clumps, 12 show an asymmetric HCO^+ profile. Although blue asymmetric line profiles are usually regarded as the signature of infall (e.g. Fuller et al. 2005), towards our clumps we see a mixture of blue asymmetric and red asymmetric profiles. Some of these clumps may be more evolved than a pure starless phase and may have already formed a protostellar core deeply embedded in the dense clump, not yet detected at 70 μm. As showed however also infalling clouds can also produce red asymmetric line profiles (Smith et al. 2013). We interpret the presence of a blue or red asymmetric line profile as an indication of dynamical activity.

Figure 2 shows the $a_{\rm k}$ vs. $a_{\rm G}$ relation for our clumps with the clumps which show asymmetric averaged HCO^+ spectra indicated. The clumps follow the $a_{\rm k}$ vs. $a_{\rm G}$ and, in agreement with the discussion in Section 3, we interpret this trend as a strong indication that, on average, the non-thermal motion in these clumps is mostly driven by self-gravity itself.

Remarkably all the clumps with gravitational acceleration $a_{\rm G} \geqslant 4.4\times10^{-14}$ g cm^{-2}, equivalent to surface density $\Sigma \geqslant 500$ M$_\odot$pc$^{-2} \cong 0.1$ g cm^{-2} show asymmetries, while only 4 over 7 clumps at lower surface densities show evidence of asymmetries. Figure 2 suggests a threshold for infall of $\Sigma_t = 500$ M$_\odot$pc$^{-2} \cong 0.1$ g cm^{-2} and so suggests this as a threshold for the gravitational instability at this clump scale for the formation of massive stars.

We recall that all our clumps are also dominated by supersonic, non-thermal motion (see Table 1). The average Mach number $\overline{\mathcal{M}}$ of the clumps with $\Sigma \geqslant \Sigma_t$ is $\simeq$ 80% higher on average than the corresponding Mach number of the less dense clumps. The same calculation for the HCO^+ asymmetric clumps shows that the average Mach number $\overline{\mathcal{M}}$ of the HCO^+ asymmetric clumps is $\simeq$ 30% higher than the corresponding Mach number in clumps with no HCO^+ asymmetries.

The presence of asymmetries in the HCO^+ spectra and higher Mach number in the dynamically active clumps are consistent with kinetic motion caused by the gravitational field. In a gravitationally driven global collapse a cloud contains a number of local centres of collapse and the chaotic motion within each cloud fragment is due to the complex geometry of the fields (Ballesteros-Paredes et al. 2011, see also Figure 1). At the beginning of the collapse, depending on the specific environment of each cloud fragment, the local turbulence can slow down the process of the star formation. The denser fragments are subject to a stronger gravitational force, therefore higher gravo-turbulent acceleration and faster collapse (e.g. Vazquez-Semadeni et al. 2007). When a particular sub-fragment reaches a high enough surface density (which Figure 2 suggests is $\Sigma_t \geqslant 0.1$ g cm^{-2}), fed by larger scale collapse, the gravitational force in the region becomes high enough to produce more ordered infall motion which is observed as high non-thermal, chaotic motion due to the complexity of the field.

Our interpretation is that in our sample the objects with HCO^+ asymmetric spectra have all evolved to this point. The sources with $\Sigma \leqslant \Sigma_t$ and HCO^+ asymmetric spectra belong to a less turbulent region and start to produce more ordered motion before the clumps with similar surface density but HCO^+ symmetric spectra. The gravitational force in all the objects above the surface density threshold Σ_t is strong enough to always produce ordered motion.

Furthermore, the force partition coefficient of the HCO^+ asymmetric clumps does not show a significant difference from the values of the HCO^+ symmetric sample: $\overline{\alpha}_{\rm for}({\rm R}_s)$=0.75 and $\overline{\alpha}_{\rm for}({\rm R}_{as})$=0.57. Similarly for clumps above and below $\Sigma_{0.1}$: $\overline{\alpha}_{\rm for}({\rm R}_{\geqslant\Sigma_{0.1}})$=0.64 and $\overline{\alpha}_{\rm for}({\rm R}_{<\Sigma_{0.1}})$=0.55. This is in agreement with the hypothesis that the force partition coefficient does not distinguish between collpasing and non collapsing regions.

Clump	RA (°)	Dec (°)	R (pc)	Σ (g cm^{-2})	σ_{nth} (km/s)	$\mathcal{M}$	$\alpha_{\rm for}\equiv\alpha_{vir}$	HCO$^+$ spectrum
MSCl15.6	18:20:29.1	-15:31:26	0.54	0.06	0.28	2.59	0.21	Sym
MSCl18.7	18:26:15.3	-12:41:33	0.69	0.22	1.07	9.82	0.57	Asym
MSCl19.2	18:27:33.9	-12:18:17	0.67	0.10	0.47	4.35	0.26	Asym
MSCl22.5	18:32:59.7	-09:20:03	0.80	0.17	1.25	11.48	0.89	Asym
MSCl22.7	18:33:49.1	-09:13:04	0.55	0.14	0.95	8.67	0.94	Asym
MSCl23.2	18:34:38.0	-08:40:45	0.72	0.14	0.94	8.65	0.69	Asym
MSCl24.0	18:33:18.5	-07:42:23	0.81	0.20	0.91	8.33	0.39	Asym
MSCl25.6	18:37:10.6	-06:23:32	0.97	0.17	1.05	9.67	0.53	Asym
MSCl25.9	18:38:54.5	-06:12:31	0.80	0.09	0.69	6.31	0.50	Sym
MSCl28.1	18:43:02.7	-04:14:52	0.85	0.23	1.07	9.79	0.45	Asym
MSCl28.5	18:44:22.0	-04:01:40	0.67	0.19	0.78	7.16	0.37	Asym
MSCl28.7	18:43:08.8	-03:36:16	0.61	0.08	0.99	9.06	1.53	Sym
MSCl30.3	18:49:40.6	-02:39:45	0.67	0.06	0.46	4.26	0.41	Asym
MSCl31.9	18:49:22.2	-00:50:32	0.82	0.14	1.19	10.87	0.94	Asym
MSCl32.0	18:51:34.1	-01:03:24	0.70	0.06	0.31	2.85	0.17	Asym
MSCl34.1	18:53:21.5	+01:06:14	0.55	0.10	0.74	6.74	0.79	Asym

Table 1. Force partition parameters of the clumps. Col. 1: name of the clumps as defined in Traficante et al. (2015, in prep.); Cols. 2-3: Coordinates of the sources, defined as the peak identified in the dust 250 μm continuum maps; Col. 4: radius of the clumps as defined by the dust continuum emission; Col.5: mass surface density derived from the FIR/sub-mm dust continuum emission; Col. 6: non-thermal component of the 1D velocity dispersion, $\sigma_{nth} = (\sigma^2_{\rm obs} - \sigma^2_{\rm th})^{1/2}$. Col.7: Mach number evaluated as $\sigma_{nth,3D}/c_s$, with $\sigma_{nth,3D} = \sqrt{3}\sigma_{nth}$ and $c_s = (k_{\rm B}T_{\rm kin}/(\mu_H m_{\rm h}))^{1/2}$. σ_{th} is evaluated from $(k_{\rm B}T_{\rm kin}/(\mu_{\rm N_2H^+} m_{\rm h}))^{1/2}$ where $k_{\rm B}$ is the Boltzmann constant, $m_{\rm h}$ the hydrogen mass and $\mu_{\rm N_2H^+}$ the mean molecular weight equal to 29.02 for N_2H^+. The gas kinetic temperature $T_{\rm kin}$ is fixed for each clump and equal to 10 K. To evaluate c_s we assume a mean hydrogen molecular weight of $\mu_H = 2.33$. Col. 6: force partition coefficient. Col. 7: keyword to identify if the clump HCO$^+$ spectrum shows a symmetric or asymmetric profile (see Section 4.1).

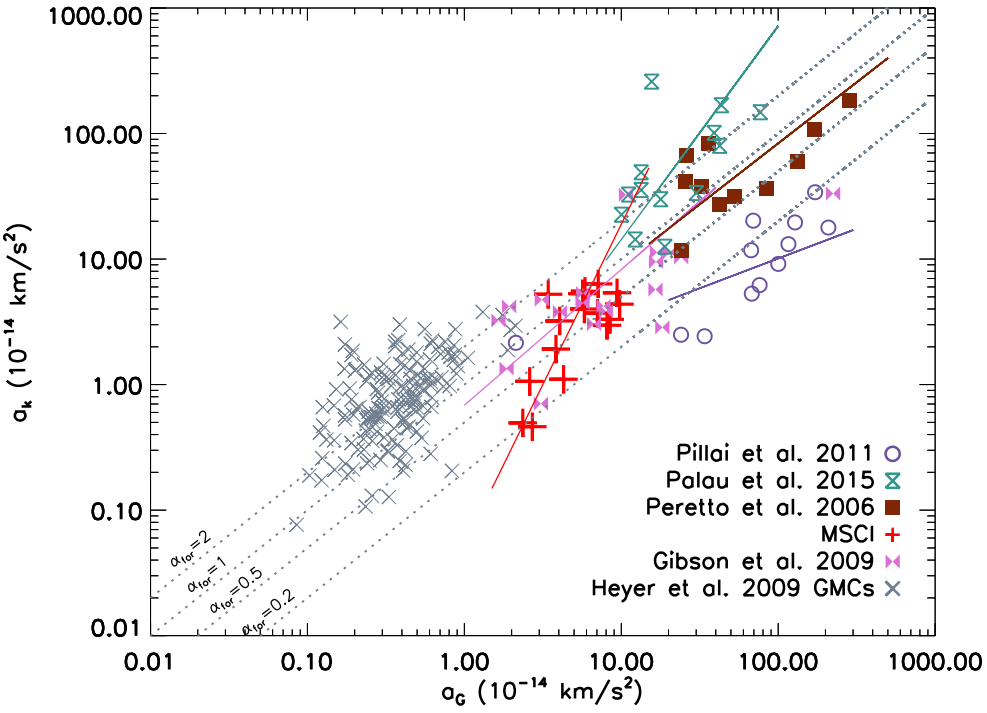

Figure 3. $a_{\rm k}$ vs.$a_{\rm G}$ relation described in Equation 2. The red plus signs are our clumps. The grey crosses are the GMC values described in H09. The light purple points are the massive clumps identified by Gibson et al. (2009). The brown points are the pre- and proto-stellar cores identified in NGC2264 by Peretto et al. (2006). The green points are the massive protostellar cores described in Palau et al. (2015). Finally, the blue circles are massive cores observed by Pillai et al. (2011). The dotted lines follow the loci of points for constant values of the force partition coefficient.

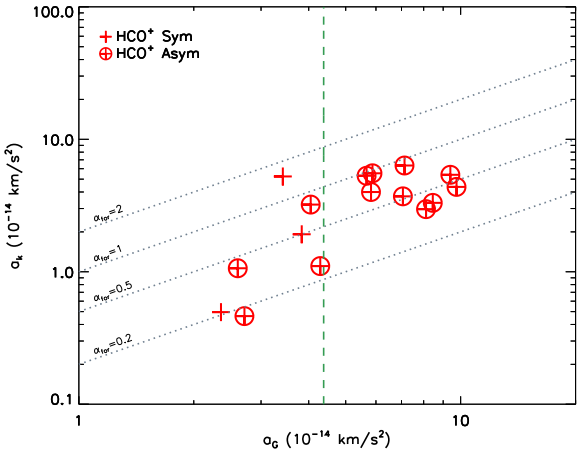

Figure 2. a_k vs. a_G diagram for our massive starless clumps. Clumps for which the HCO^+ spectrum is asymmetric are shown as circled plus signs. All of the clumps with $a_{Gt} \geqslant 4.4{\times}10^{-14}$ g cm^{-2} $\equiv \Sigma \geqslant 500$ M$_\odot$pc^{-2} $\cong$ 0.1 g cm^{-2} (the green-dotted line) shows signs of ordered gravitational collapse, while only 4 of the 7 clumps below this threshold shows similar signs. The grey-dotted lines follow the loci of points for constant values of the force partition coefficient.

5 GRAVITATIONAL FORCE DRIVING THE KINETIC MOTION IN MASSIVE STAR FORMING REGIONS

In Figure 3 we plot the a_k vs. a_G relation including data for GMCs, our clumps and massive cores at different evolutionary stages from the literature.

We can identify three distinct loci of points in the plot:

1. The large, relatively low density GMCs traced with ^{13}CO which occupy the left-hand side of the diagram. The points show the GMC data of the cloud as a whole (size 10-100 pc) discussed in H09. We did not include cloud values interpolated within the half-power isophote of the column density (size 1-30 pc) as in the original work of H09, as we are interested in the region of the diagram occupied by the clouds as a whole.

There is a large dispersion in the a_k vs. a_G plane for the GMCs, and there is no evident relation between a_k and a_G at the GMCs scale. The average force partition coefficient for the GMCs sample is $\alpha_{GMC} = 1.9$ (H09) with many clouds having $\alpha_{GMC} > 2$. Most of clouds appear unbound on large scales. This value is higher than the average value of α_{for} found in our clumps and in massive young cores as discussed in the next paragraphs. There are three possible explanations of the GMCs distribution analysed in the literature (e.g. H09; Field et al. 2011; Dobbs et al. 2011). First, the mass could be underestimated by a factor of 2-3 due to the LTE approximation and the assumption of constant CO abundance. If this hypothesis is correct then the force partition coefficient of the GMCs becomes similar on average to the value of our clumps and massive cores. Second, the mass estimation is correct and the majority of the clouds are unbound and will never collapse. Only the clouds and cloud fragments with $\alpha_{vir} \leqslant 2$ will collapse and form clumps and cores (Dobbs et al. 2011). This interpretation however is consistent with a standard virial analysis, in which all the velocity dispersion is attributed to turbulence. In the gravo-turbulent formalism we cannot resolve the origin of non-thermal motions in single clouds, as discussed in Section 3. If this hypothesis is correct the majority of GMCs (all clouds with $\alpha_{for} \geqslant 2$) do not have enough gravitational force to act against local turbulence and they will dissolve, while we can not reach any conclusion for clouds with $\alpha_{for} \leqslant 2$. Finally, there is the contribution of the external pressure as an additional confining force that needs to be taken into account (Field et al. 2011). In Section 6 we discuss the implications of accounting for external pressure in Equation 2.

2. The central region of the diagram is occupied by our massive clumps and the sources from Gibson et al. (2009) who analyzed a sample of massive cores and clumps (size 0.6-4.0 pc) selected to be dark at 8 μm and observed with CS emission line, a tracer of dense gas in star forming regions. This dataset, combined with the H09 data were used in Ballesteros-Paredes et al. (2011) to discuss their global collapse model. Both these surveys of massive clumps show a clear increasing of a_k at the increasing of a_G. The straight lines are the best linear fit in the log-log space for the two surveys. The fit was done with the `linfitex` IDL routine accounting for errors in both the estimation of a_k and a_G. We consider an error of 40% in the estimation of the mass surface density (i.e. a_G) and an error of 40% in the velocity dispersion and radius (i.e. a_k) estimations. The slope in the log-log space gives $A_{MSCl} = 2.55 \pm 1.03$ and $A_{Gib.} = 1.08 \pm 0.25$ for our MSCls clumps and the Gibson et al. (2009) clumps respectively. Noticeably, the values of the coefficient are slightly higher than (or compatible with, for the Gibson et al. (2009) sample) 1, which would correspond to the expected power law slope in case of constant value of the force partition parameter going towards region of higher surface density, e.g. a linear increase of a_k at increasing a_G.

3. The locus of points occupied by different surveys in the literature of young prestellar and protostellar cores. The brown points are dense cores (size 0.03-0.05 pc) embedded in the massive clumps NGC2264 C and D observed by Peretto et al. (2006). The surface density of each core has been evaluated from the size and mass in Table 2 of Peretto et al. (2006). We used the data for the 11 resolved cores with a well defined core radius. These clumps are located in the Mon OB-1 molecular cloud complex at $d \simeq 800$ pc and here we refer to the results from the N_2H^+ (1 – 0) data obtained with IRAM 30m. The young cores traced with N_2H^+ mostly lie below $\alpha_{BE,cr} = 2$, and the majority of them significantly below $\alpha_{cr} = 1$. The locus of points of these massive cores show similar force partition coefficient to our starless clumps. The blue circles are pre-protoclusters observed with NH_2D in G29.960.02 and G35.201.74 (W48) by (Pillai et al. 2011) using the Plateau de Bure Interferometer. Finally, the green points are a sample of 13 evolved cores observed in NH_3 (1 – 1) with the Very Large Array (VLA) by Palau et al. (2015). We estimated the mass surface density assuming the core masses in Table 1 of Palau et al. (2015) and assuming a core radius of 0.05 pc as described in Palau et al. (2015). These more evolved cores, actively forming stars, lie close to or above the virial BE limit $\alpha_{vir} = 2$ perhaps due to the line-width of the NH_3 (1 – 1) being broadened by the passage of outflows (Sánchez-Monge et al. 2013; Palau et al. 2015). We note that if we use the velocity dispersion of the N_2H^+ data taken at IRAM 30m for this sample (Palau et al. 2015), the locus of points does not differ, even though the velocity dispersion is smaller than that of the NH_3 (Palau et al. 2015). The linear fit for these samples give power law slopes of $A_{Per.} = 0.97 \pm 0.98$, $A_{Pil.} = 0.47 \pm 0.15$ and $A_{Pal.} = 1.70 \pm 1.54$ for the samples of Peretto et al. (2006), Pillai et al. (2011) and Palau et al. (2015) respectively, consistent with an increasing of gravo-turbulent acceleration towards region of higher surface densities.

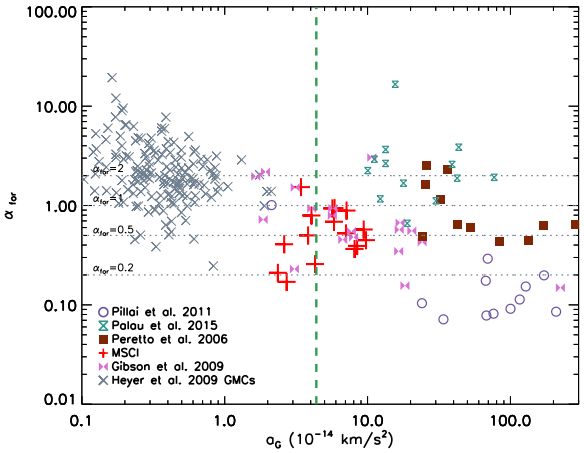

Figure 4. Force partition coefficient as a function of the gravitational force for the same objects shown in Figure 3. There is no clear evidence for a trend of $\alpha_{\rm for}$ with $a_{\rm G}$ (surface density). The green dotted line delimits the $\Sigma_t \geqslant 0.1$ g cm^{-2} region. The grey dotted lines show constant values of $\alpha_{\rm for}$.

From Figure 3 it is evident that within each survey $a_{\rm k}$ *consistently* increases with increasing $a_{\rm G}$.

There is no clear distinction of the force partition coefficients between objects at different evolutionary stages. To emphasize this in Figure 4 we show the clouds and cloud fragments in the $\alpha_{\rm for}$ vs. Σ plane. The green dotted vertical line indicates the $\Sigma_t = 0.1$ g cm^{-2} surface density threshold. Clouds and cloud fragments span a wide range of $\alpha_{\rm for}$ at all scales and there is no evident distinction in the $\alpha_{\rm for}$ vs. Σ plane below and above Σ_t.

The different values of the force partition coefficient in the same survey shown in Figure 4 may depend on different values of the ambient pressure, magnetic fields, and uncertainties, but may not be related with equilibrium. The majority of the non-thermal motion must in fact arise from the gravitational force as shown in Figure 3. Similar conclusions have been obtained from Hernandez & Tan (2015) who analyzed a sample of 10 massive IRDCs with ^{13}CO emission. They found a strong correlation in the H09 $\sigma/{\rm R}^{1/2}$ vs. Σ diagram, which is equivalent to our diagram in Figure 3. Although they found their sample shows dynamic signatures compatible with the turbulent core/clump/cloud model of McKee & Tan (2003), the correlation in the H09 diagram may represent a self-similar hierarchy of self-gravitating virialized structures (Hernandez & Tan 2015).

There is also an indication from Figure 3 of an evolutionary trend, with $a_{\rm k}$ that increases with increasing $a_{\rm G}$ in a similar fashion from the scales of large clumps (and maybe GMCs) down to the cores in massive star forming regions. However the direct comparison between different surveys is difficult due to uncertainties and systematic effects which arise from the comparison of different datasets. Different tracers may look at different regions along the line of sight and the line broadening may be affected differently for each gas tracer/stage of evolution (e.g. Palau et al. 2015). The estimated value of $\alpha_{\rm for}$ for clouds or cloud fragments in each survey may be significantly affected by the chosen tracer. Furthermore, the increase of the force partition coefficient with decreasing gravitational force in GMCs may be explained, as we show in the next Section, by the contribution of the external pressure.

6 EXTERNAL PRESSURE

If clouds are pressure confined, Equation 2 must be modified to account for the pressure contribution which increases the observed non-thermal motion. In the standard virial analysis the pressure term can be added to Equation 2 as (Field et al. 2011):

$$\frac{\sigma^2}{\rm R} = \alpha_{\rm vir}\frac{\pi G\Sigma}{5} + \frac{4P_{ext}}{3\Sigma}. \quad (3)$$

In the gravo-turbulent formulation Equation 3 becomes:

$$a_{\rm k} = \alpha_{\rm for}\, a_{\rm G} + \frac{4\pi G}{15}\frac{P_{ext}}{a_{\rm G}} \equiv \widehat{\alpha}_{\rm for}(a_{\rm G})\, a_{\rm G} \quad (4)$$

with

$$\widehat{\alpha}_{\rm for}(a_{\rm G}) = \alpha_{\rm for}\left(1 + \frac{4\pi G}{15\alpha_{\rm for}}\frac{P_{ext}}{a_{\rm G}^2}\right). \quad (5)$$

Equation 4 implies that $a_{\rm k}$ will not be proportional to only the gravitational force where the external pressure dominates or when the gravitational force is sufficiently low. Equation 5 shows the force partition coefficient $\widehat{\alpha}_{\rm for}$ of a pressure confined cloud (or cloud fragment) is greater than $\alpha_{\rm for}$ in absence of external pressure for the same region. For large values of $a_{\rm G}$ the terms $\propto a_{\rm G}^{-2}$ in Equation 4 goes rapidly to zero and $\widehat{\alpha}_{\rm for} \longrightarrow \alpha_{\rm for}$.

The theoretical value of the external pressure generated by the neutral ISM and required to confine a molecular cloud is of the order of $P_{ext}/k \simeq 10^4$ K cm^{-3} (Elmegreen 1989). Observations of individual regions show a range of values, from $P_{ext}/k = 5\times10^4$ K cm^{-3} (Bertoldi & McKee 1992) to $P_{ext}/k = 5\times10^5$ K cm^{-3} in nearby starless cores (Belloche et al. 2011).

In Figure 5 we show the same data points of Figures 3 and 4, this time including the loci of points occupied by the solution of Equation 3 for two different values of external pressure, $P_{ext}/k = 10^4$ and $P_{ext}/k = 10^5$ K cm^{-3}, (the straight and the dot-dashed line respectively) and for various values of $\alpha_{\rm for}$. The figure shows that with a contribution of an external pressure of e.g. $P_{ext}/k = 10^4$ K cm^{-3} at $a_{\rm G} \lesssim 2\times10^{-14}$ km s^{-2}, the collapse is driven by the external pressure. At $a_{\rm G} \geqslant 2\times10^{-14}$ km s^{-2} gravity starts to dominate and the kinetic force increases again with increasing gravitational force at all scales, from GMCs down to cores. We note that $a_{\rm G} \simeq 2\times10^{-14}$ km s^{-2} $\equiv \Sigma \simeq 0.04$ g cm^{-2}, the threshold discussed in McKee et al. (2010) and Tan et al. (2014) above which the gravity dominates the motion in star forming regions and the cloud and cloud fragments follow Equation 2.

For a cloud with $\Sigma = 0.01$ g cm^{-2} $\equiv a_{\rm G} = 0.42\times10^{-14}$ km s^{-2} and, in absence of external pressure, $\alpha_{\rm for}$=0.5 the corresponding gravo-turbulent acceleration will be $a_{\rm k} \simeq 0.2\times10^{-14}$ km s^{-2}. If we include a contribution of an external pressure of $P_{ext}/k = 5\times10^4$ K cm^{-3} we will measure $a_{\rm k} \simeq 1.1\times10^{-14}$ km s^{-2} and $\widehat{\alpha}_{\rm for} \simeq 5.7$. The high gravo-turbulent acceleration observed in GMCs can be therefore explained by motion induced by an external pressure. This picture supports that the majority of the GMCs could globally collapse, initially under the confinement of the external pressure and a negligible contribution of the gravitational force. As the surface density increases, the gravity becomes dominant at all scales and the gravo-turbulent acceleration increases quasi-linearly with the gravitational force of the cloud.

7 MAGNETIC FIELDS

Magnetic fields can also act as a large scale support against gravity. In the virial analysis they can prevent collapse in clumps with

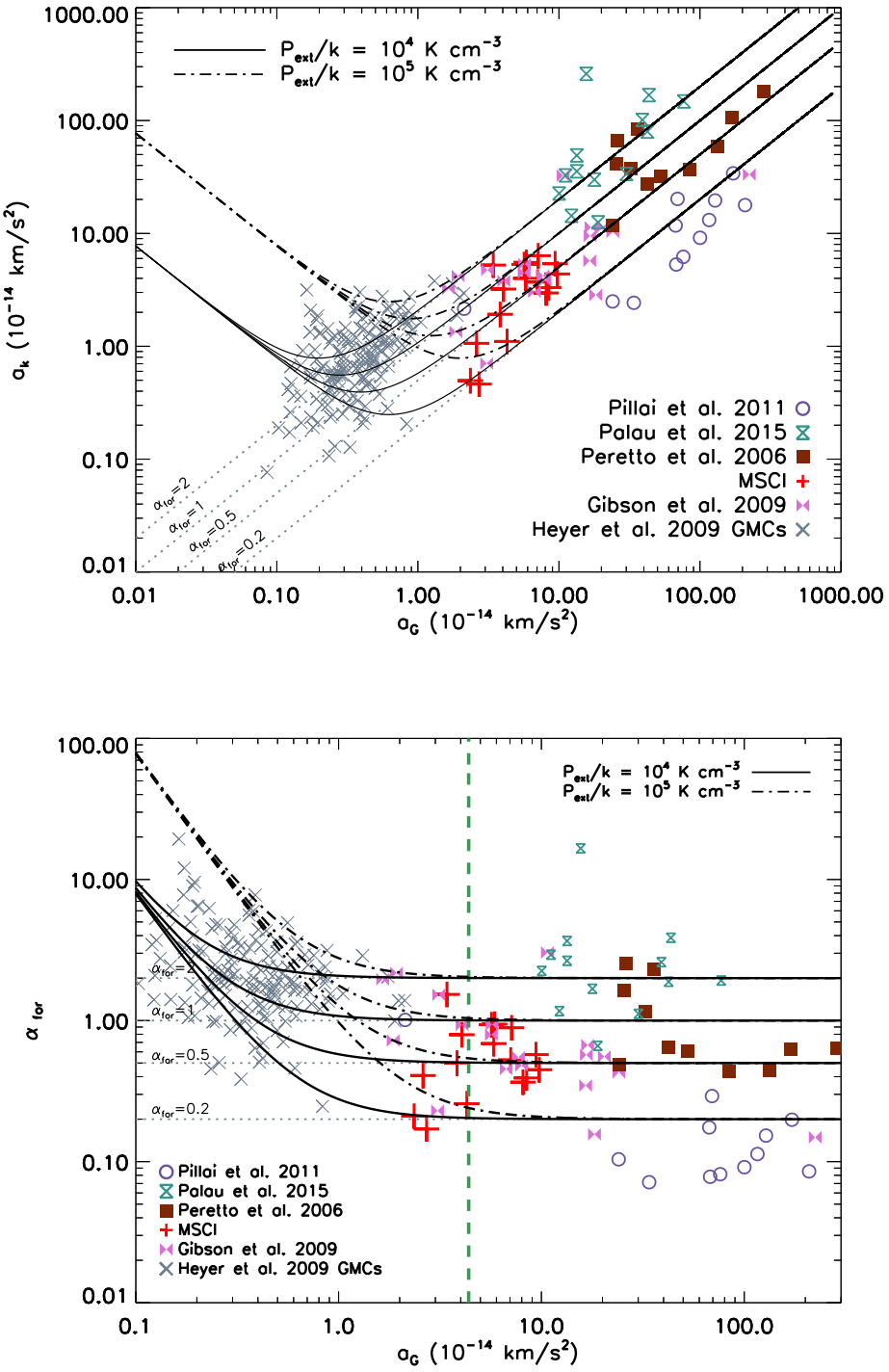

Figure 5. Same of Figures 3 and 4 including the solutions of Equation 4 for two different values of the external pressure and for fixed values of $\alpha_{\rm for}$.

α_{vir}<< 2 (Bertoldi & McKee 1992; Tan et al. 2013). If we include the magnetic field as support against gravitational collapse of a hydrostatic isothermal sphere we obtain (Kauffmann et al. 2013):

$$B_{eq} = 81\mu{\rm G}\frac{M_\Phi}{M_{\rm BE}}\left(\frac{\sigma_{\rm N_2H^+}}{\rm kms^{-1}}\right)^2\left(\frac{R}{\rm pc}\right)^{-1} \quad (6)$$

where M_Φ is the magnetic flux mass for a field of mean strength $\langle B_{eq}\rangle$ (Tomisaka et al. 1988), $M_{\rm BE}$ the Bonnor-Ebert mass (see Section 1) and $M_\Phi/M_{\rm BE} \simeq 2/\alpha_{vir} - 1$ (Kauffmann et al. 2013).

Crutcher (2012) shows there is an upper limit of the intensity of the magnetic field B_{up} in a given region which depends on the particle density $B_{up} \simeq 150\ \mu$G $(n_{\rm H_2}/10^4\ {\rm cm^{-3}})^{0.65}$. If we assume

spherical geometry and density equal to the mean density, B_{up} can be rewritten as (Kauffmann et al. 2013):

$$B_{up} \simeq 336\,\mu\mathrm{G}\left(\frac{M}{10M_{\odot}}\right)^{0.65}\left(\frac{R}{0.1\ \mathrm{pc}}\right)^{-1.95} \quad (7)$$

The strength of the magnetic field required to sustain each clump against collapse can be compared with the critical value B_{up}. In Table 2 we report the intensity of the magnetic fields required for each clump to reach the BE equilibrium, the critical value B_{up} and the ratio between the two, separating the clumps above and below the surface density threshold.

The mean intensity of the magnetic field required to maintain the equilibrium in the clumps above the surface density threshold is $\overline{B} = 230 \pm 93\ \mu$G, while the value for the clumps below is $\overline{B} = 99 \pm 43\ \mu$G. B_{up} is close to or smaller than the intensity of the magnetic field required to sustain the collapse for all the clumps with $\Sigma_t \geqslant 0.1$ g cm^{-2}, and for all but 1 non-collapsing clumps (MSCl28.7). At $\Sigma \geqslant 0.1$ g cm^{-2} the average value of the ratio $\frac{B_{eq}}{B_{up}}$ is $\simeq$1.50 while at lower surface densities the average value of the ratio $\frac{B_{eq}}{B_{up}}$ is $\simeq$1.06. The magnetic fields are likely not sufficient to prevent the collapse driven by the strong gravitational field in the majority of these MSCls, in particular in the higher surface density clumps. There are large uncertainties on these estimations, however. For example, the assumption of spherical geometry with a mean density value may not be representative. Assuming a factor of 2 of uncertainty in the estimation of B_{eq} and B_{up}, the majority of the high surface density clumps require a moderately strong magnetic field to sustain an equilibrium, and the value of B_{eq} should be close to the upper limit suggested by Crutcher (2012). These values are comparable to the intensities of the magnetic fields estimated by Tan et al. (2013) to maintain the virial equilibrium of their starless cores with $\alpha_{vir} \leqslant 1$.

The strong magnetic fields required to prevent the collapse of high mass surface density regions have a direct interpretation in the gravo-turbulent formulation of the star formation mechanism. Equation 6 has an explicit dependence on the quantity $\sigma^2/\mathrm{R} \equiv a_{\mathrm{k}}$. Since the role of the magnetic fields is to slow-down the collapse, for a given value of the gravo-turbulent acceleration we can estimate the intensity of the magnetic field required to sustain the gravity against the collapse assuming that all the non-thermal motion originates from self-gravity.

If we invert Equation 6 and rewrite it as function of the gravo-turbulent acceleration:

$$a_{k,B_{eq}} = 3.24 \cdot 10^{-14}\ \mathrm{km\ s^{-2}}\ \frac{B_{eq}}{81\mu\mathrm{G}}\ \frac{M_{\mathrm{BE}}}{M_{\Phi}} \quad (8)$$

where we can define $a_{k,B_{eq}}$ as the gravo-turbulent acceleration that can be sustained against the collapse by a given magnetic field B_{eq}. However in Section 3 we showed that a_{k} increases at increasing a_{G}. Equation 8 shows that we need higher magnetic fields to prevent the collapse at higher a_{k}, which implies higher mass surface densities (i.e. higher a_{G}).

Similarly, if we substitute B_{up} at B_{eq} in Equation 8 we get an estimate of the maximum acceleration that can be counter-balanced by the highest magnetic field allowed for each clump $a_{k,B_{up}}$. From Equation 8 follows:

$$\frac{a_{k,B_{eq}}}{a_{k,B_{up}}} \equiv \frac{B_{eq}}{B_{up}} \quad (9)$$

Therefore $a_{k,B_{eq}}/a_{k,B_{up}} \gtrsim 1$ for all but 1 clump (see Table 2) and the magnetic fields cannot prevent these clumps from the collapse.

Clump	Type	B_{eq} (μG)	B_{up} (μG)	$\frac{B_{eq}}{B_{up}}$
MSCl18.7	Asym	337	211	1.6
MSCl22.5	Asym	197	161	1.2
MSCl22.7	Asym	150	175	0.9
MSCl23.2	Asym	189	151	1.2
MSCl24.0	Asym	342	177	1.9
MSCl25.6	Asym	260	141	1.8
MSCl28.1	Asym	376	188	2.0
MSCl28.5	Asym	324	195	1.7
MSCl31.9	Asym	158	140	1.1
MSCl15.6	Sym	108	100	1.1
MSCl19.2	Asym	186	129	1.4
MSCl25.9	Sym	145	108	1.3
MSCl28.7	Sym	40	117	0.3
MSCl30.3	Asym	104	93	1.1
MSCl32.0	Asym	120	92	1.3
MSCl34.1	Asym	124	141	0.9

Table 2. Magnetic fields estimation separated for clumps above and below the surface density threshold $\Sigma = 0.1$ g cm^{-2}. Col. 1: name of the clumps as defined in Traficante et al. (2015, in prep.); Col. 2: keyword to identify clumps which show symmetric (Sym) or asymmetric (Asym) HCO^+ spectra. Col. 3: Intensity of the magnetic field required to reach BE equilibrium, B_{eq}. Col. 4: Maximum intensity of the magnetic field as estimated following Crutcher (2012), B_{up}. Ratio between B_{eq} and B_{up}.

8 CONCLUSIONS

In this work we demonstrated that the Heyer relation is a direct consequence of a gravo-turbulent description of the non-thermal motions in collapsing clouds and cloud fragments. We introduced a new coefficient, the force partition coefficient α_{for}, defined as ratio between the gravitational acceleration a_{G} and a gravo-turbulent acceleration a_{k}, the former defined as function of the mass surface density and the latter as function of the velocity dispersion and the radius of the cloud or cloud fragment.

We explored the implications of this new formalism and compared the predictions with the analysis of the kinematics of a sample of 16 massive starless clumps identified in IRDCs in the Hi-GAL survey. The clumps have been selected to be "quiescent" (dark or very faint at 70 μm, L/M$<$ 0.3), avoiding any line-broadening due to stellar feedback. The gravo-turbulent mechanism has been further explored with the analysis of surveys of GMCs, clumps and pre- and proto-stellar cores from the literature.

This new formalism and the results we obtained have several implications for understanding how massive stars are formed:

1. The non-thermal motions observed in clouds and cloud fragments originates from both local turbulence acting against the gravity and the self-gravity. The two components cannot be observationally separated. The observed gravo-turbulent acceleration is not independent from the gravitational acceleration. The data show increasing a_{k} at the increasing of a_{G} from the scales of clumps (and possibly GMCs) down to the cores, independent of the α_{for} values of the single regions. The gravo-turbulent formulation shows that on average the self-gravity, and not the local turbulence, drives much of the observed non-thermal motion.

2. The force partition coefficient $\alpha_{\rm for}$ is equivalent to the virial parameter. The most important difference is that $\alpha_{\rm for}$ does not distinguish between regions in equilibrium or not. $\alpha_{\rm for}$=2 is a theoretical upper limit for collapsing regions in absence of magnetic fields and external pressure (equivalently to $\alpha_{\rm BE}$). However $\alpha_{\rm for} \leqslant 2$ does not necessarily determine the stability of regions analyzed singularly, as the observed non-thermal motion can arise from local turbulence or chaotic global collapse.

3. All clumps with a surface density $\Sigma \geqslant 500$ M$_\odot$ pc^{-2} $\cong$ 0.1 g cm^{-2} show signs of ordered gravitational collapse, while not all clumps with $\Sigma \leqslant 0.1$ g cm^{-2} show these signs, independent of the value of $\alpha_{\rm for}$. We interpret these results as evidence that the densest clumps are those least affected by local turbulence and the first to collapse.

4. Including an external pressure of $\simeq 10^4 - 10^5$ P_{ext}/k which confines the GMCs explains the high values of the gravo-turbulent acceleration observed in these clouds and does not exclude that the majority of them are globally collapsing. The contribution of the external pressure can be incorporated in the formalism of the gravo-turbulent mechanism, modifying the definition of $\alpha_{\rm for}$.

5. Magnetic fields, if present, can act as a support against the global collapse. We showed that magnetic fields stronger than the maximum intensity of the magnetic field suggested by Crutcher (2012) are required to sustain the majority of the massive starless clumps, which are all (but one) unstable. We also showed that stronger magnetic fields required to sustain higher surface density regions are explained by the gravo-turbulent description of the global collapse mechanism.

The gravo-turbulent formulation and the $a_{\rm k}$ vs. $a_{\rm G}$ relation, if confirmed at all scales, may have a great impact on our understanding of the massive star formation mechanism. If the global collapse mechanism with the gravity driving much of the non-thermal motion is correct and the strength of the magnetic field is not sufficient we would expect to observe pure thermal Jeans fragmentation in most of the clumps. This hypothesis can be explored in the near future using high-resolution instruments such as NOEMA or ALMA.

ACKNOWLEDGEMENTS

This work has benefited from research funding from the European Community's Seventh Framework Programme. AT is supported by STFC consolidated grant to JBCA. AT wants to thank J. Ballesteros-Paredes and E. Vazquez-Semadeni for their inspiring works and S. Camera for the stimulating conversations at the origin of this work.

REFERENCES

Aguirre J. E., Ginsburg A. G., Dunham M. K., et al. 2011, ApJS, 192, 4
Ballesteros-Paredes J., Hartmann L. W., Vázquez-Semadeni E., et al. 2011, MNRAS, 411, 65
Belloche A., Schuller F., Parise B., et al. 2011, A&A, 527, A145
Bertoldi F., McKee C. F., 1992, ApJ, 395, 140
Crutcher R. M., 2012, ARAA, 50, 29
Dobbs C. L., Burkert A., Pringle J. E., 2011, MNRAS, 413, 2935
Elmegreen B. G., 1989, ApJ, 338, 178
Field G. B., Blackman E. G., Keto E. R., 2008, MNRAS, 385, 181
Field G. B., Blackman E. G., Keto E. R., 2011, MNRAS, 416, 710
Fuller G. A., Williams S. J., Sridharan T. K., 2005, A&A, 442, 949
Gibson D., Plume R., Bergin E., et al. 2009, ApJ, 705, 123
Hernandez A. K., Tan J. C., 2015, arXiv.org, p. 183
Heyer M. H., Brunt C. M., 2004, ApJ, 615, L45
Heyer M. H., Krawczyk C., Duval J., et al. 2009, ApJ, 699, 1092
Jackson J. M., Rathborne J. M., Shah R. Y., et al.. 2006, ApJS, 163, 145
Kauffmann J., Pillai T., Goldsmith P. F., 2013, ApJ, 779, 185
Krumholz M. R., Tan J. C., 2007, ApJ, 654, 304
Larson R. B., 1981, MNRAS, 194, 809
McKee C. F., Li P. S., Klein R. I., 2010, ApJ, 720, 1612
McKee C. F., Ostriker E. C., 2007, ARAA, 45, 565
McKee C. F., Tan J. C., 2003, ApJ, 585, 850
Molinari S., Swinyard B., Bally J., et al. 2010, PASP, 122, 314
Padoan P., Nordlund Å., 2002, ApJ, 576, 870
Palau A., Ballesteros-Paredes J., Vazquez-Semadeni E., et al. 2015, ArXiv e-prints
Peretto N., Andre P., Belloche A., 2006, A&A, 445, 979
Peretto N., Fuller G. A., 2009, A&A, 505, 405
Peretto N., Fuller G. A., Duarte-Cabral A., et al. 2013, A&A, 555, A112
Peretto N., Fuller G. A., Plume R., et al. 2010, A&A, 518, L98+
Pillai T., Kauffmann J., Wyrowski F., et al. 2011, A&A, 530, A118
Sánchez-Monge Á., Palau A., Fontani F., et al. 2013, MNRAS, 432, 3288
Sanhueza P., Jackson J. M., Foster J. B., et al. 2012, ApJ, 756, 60
Schuller F., Menten K. M., Contreras Y., et al. 2009, A&A, 504, 415
Smith R. J., Shetty R., Beuther H., et al. 2013, ApJ, 771, 24
Solomon P. M., Rivolo A. R., Barrett J., et al. 1987, ApJ, 319, 730
Tan J. C., Beltrán M. T., Caselli P., et al. 2014, Protostars and Planets VI, pp 149–172
Tan J. C., Kong S., Butler M. J., et al. 2013, ApJ, 779, 96
Tomisaka K., Ikeuchi S., Nakamura T., 1988, ApJ, 335, 239
Traficante A., Fuller G. A., Peretto N., et al. 2015, MNRAS, 451, 3089
Urquhart J. S., Moore T. J. T., Csengeri T., et al. 2014, MNRAS, 443, 1555
Vasyunina T., Linz H., Henning T., et al. 2011, A&A, 527, 88
Vazquez-Semadeni E., Gómez G. C., Jappsen A. K., et al. 2007, ApJ, 657, 870
Vázquez-Semadeni E., Gómez G. C., Jappsen A.-K., et al. 2009, ApJ, 707, 1023
Wilcock L. A., Ward-Thompson D., Kirk J. M., et al. 2012, MNRAS, 422, 1071

APPENDIX A: HCO$^+$ SPECTRA

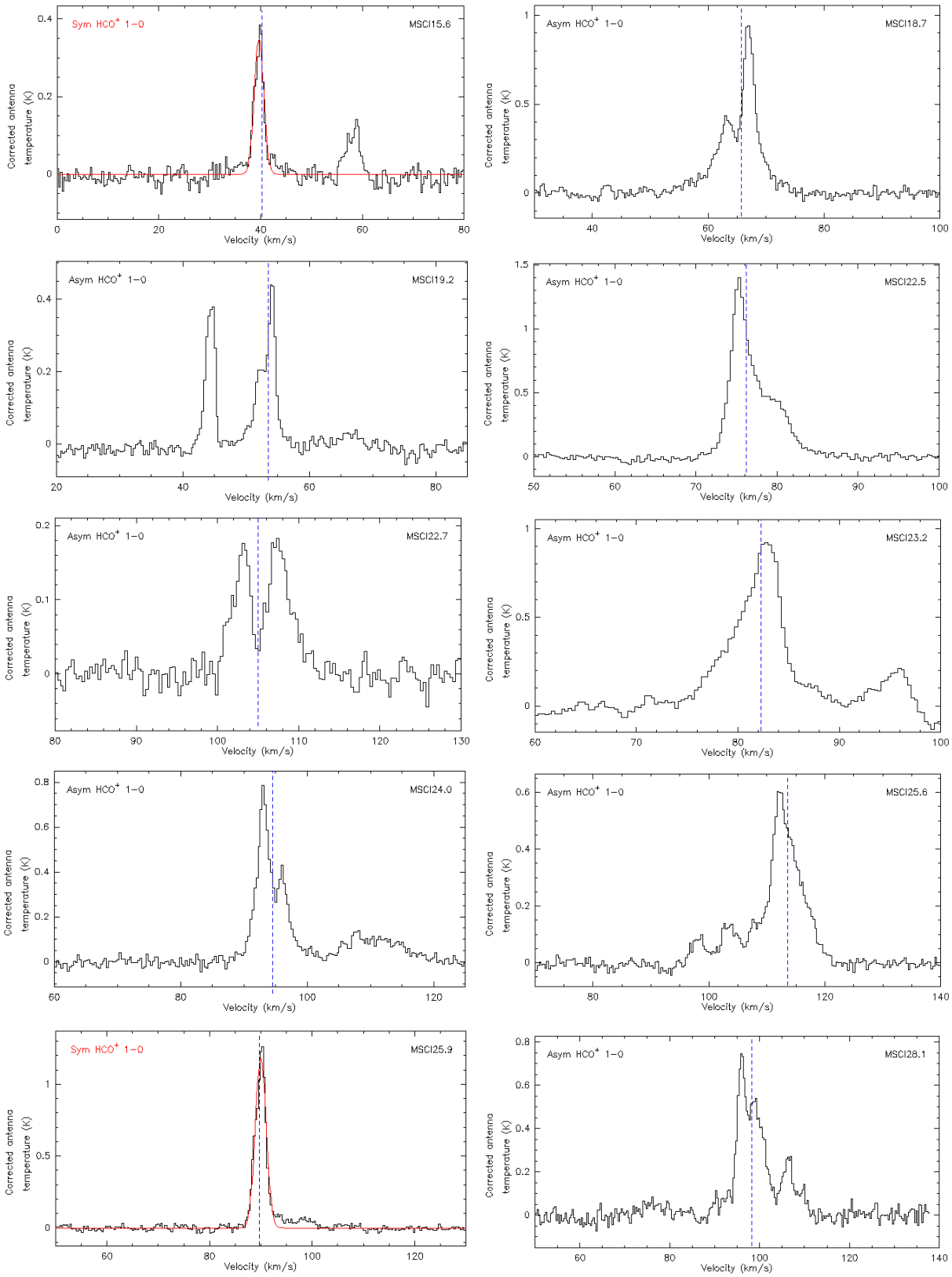

Figure A1. HCO^+ spectra of the 16 MSCl obtained for each clump as described in Section 4. The clumps which do not show signs of HCO^+ asymmetries are indicated in red, with a Gaussian fit of the HCO^+ profile obtained with the `gauss` task in CLASS. They are MSCl15.6, MSCl25.9 and MSCl28.7. The detail analysis of the HCO^+ spectra parameters are in Traficante et al. (2015, in prep.).

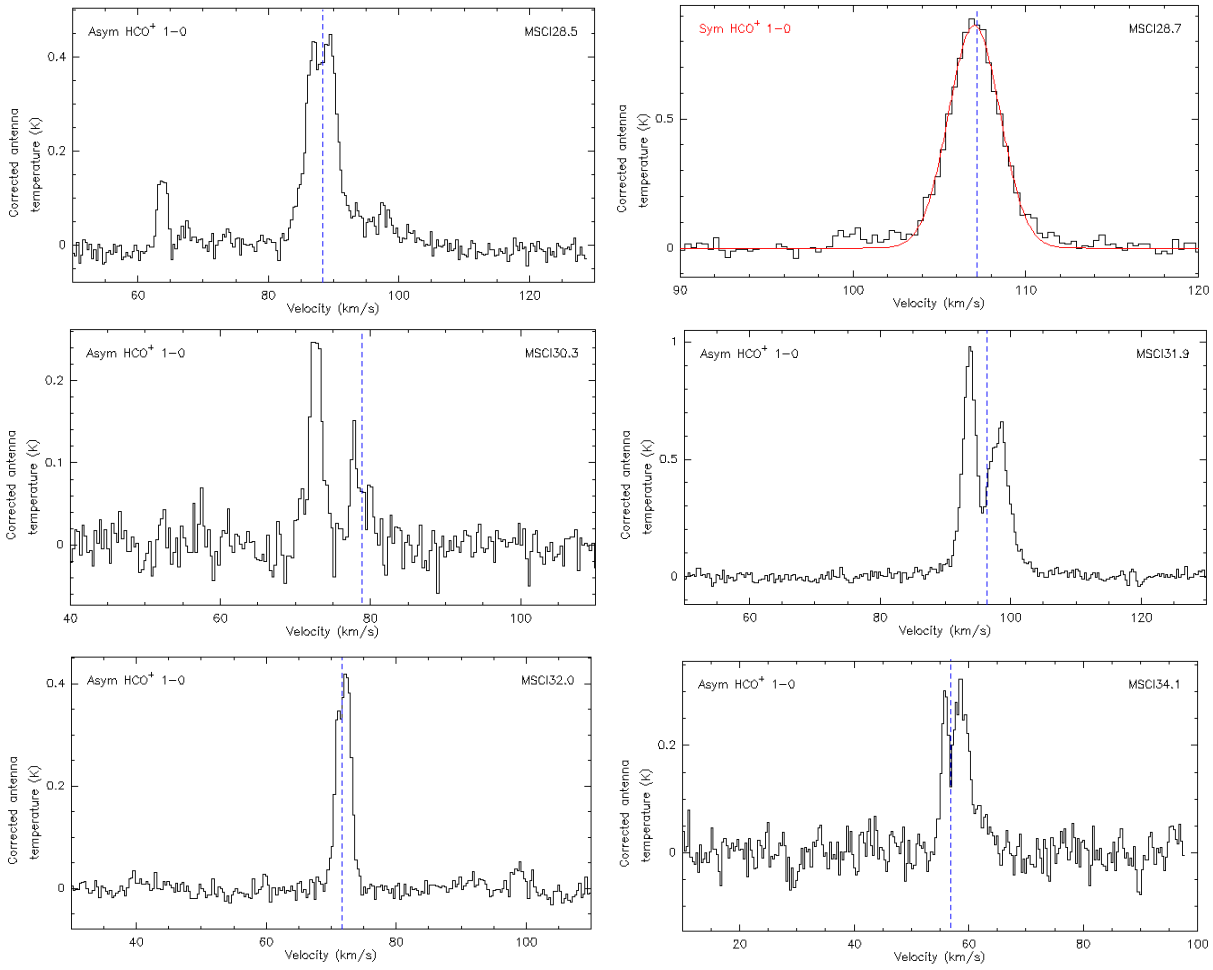

Figure A2. Figure A1 continued.